Icarus 269 (2016) 38–49

Contents lists available at ScienceDirect

Icarus

journal homepage: www.elsevier.com/locate/icarus

Radar scattering by planetary surfaces modeled with laboratory-characterized particles

A. Virkki[a,*], K. Muinonen[a,b]

[a] Department of Physics, University of Helsinki, P.O. Box 64, FI-00014, Finland
[b] Finnish Geospatial Research Institute, Geodeetinrinne 2, Masala FI-02431, Finland

ARTICLE INFO

Article history:
Received 28 September 2015
Revised 28 December 2015
Accepted 8 January 2016
Available online 14 January 2016

Keywords:
Asteroids
Composition
Surfaces
Radar observations
Radiative transfer

ABSTRACT

We model radar scattering by planetary surfaces using a ray-optics algorithm that includes Fresnelian reflection and refraction, diffuse scattering, and coherent backscattering. We enhance the realism of the ray-optics algorithm by using scattering particles that are geometrically representative of the surfaces and interiors of planetary bodies. The shapes as well as the dielectric properties of the scattering particles have been characterized in laboratory. The results demonstrate the effects of various physical parameters on radar scattering with an emphasis on asteroids. We present the effects of number density, size distribution, and dielectric and geometric properties of scattering particles on the radar reflectivity and circular-polarization ratio of planetary surfaces. We also briefly discuss applications to the Galilean Moon Europa and comets.

1. Introduction

During the last few decades, a vast literature describing the radar scattering properties of various Solar System objects has accumulated. Simultaneously, there is a shortage of work on what the observations imply about the physical properties of the diverse planetary surfaces. We simulate radar scattering using an algorithm of ray optics and diffuse scattering. We enhance the realism by using scattering particles that are geometrically representative of the surfaces and interiors of planetary bodies. Thus, we can simulate multiple scattering in planetary surfaces, including dust, boulders, or broken rock or ice more accurately than has been done before.

In the modern radar observations, the most common setup for the transmitted signal is a fully circular polarization with a frequency of 2380 MHz (S band, the wavelength $\lambda = 12.6$ cm) or 8560 MHz (X band, $\lambda = 3.5$ cm). The echo can be received simultaneously in the same (SC) and opposite circular (OC) polarization states as compared to the state of the echo originally transmitted.

The echo power in the SC sense depends substantially on the physical properties of the target. For example, in a simple reflection at normal incidence on an interface between two isotropic, dielectric media that is either planar or has a radius that greatly exceeds the wavelength of the incident radiation, the handedness of the circular polarization turns fully. Craters, boulders, or any wavelength-scale irregularities, on the other hand, cause part of the radiation to remain in the original helicity. Therefore, the ratio of the echo power in the SC sense to that in the OC sense, i.e., the circular-polarization ratio, has traditionally been used as a measure of the target's near-surface, wavelength-scale geometric complexity, or "roughness" (Ostro et al., 2002).

Currently, data for about 700 asteroids have been obtained using planetary radar. Fig. 1 illustrates observational data for 120 asteroids, for which both the circular polarization ratio and the (OC) radar albedo have been published.

As Fig. 1 demonstrates, in some cases the circular-polarization ratio depends on the spectral taxonomy type of the asteroid, which has been measured on optical and infrared wavelengths. As well, the mean circular-polarization ratio of the near-Earth asteroids (NEAs) is higher than that of the main-belt asteroids (MBAs), as shown by, e.g., Benner et al. (2008). The variation of the circular-polarization ratios between the different spectral or population types are explained by the dependence of the surface roughness on the type, which is related to how the asteroid has formed (Benner et al., 2008; Shepard et al., 2008b). As well, the circular-polarization ratio can vary substantially even locally, within some specific asteroids (Virkki et al., 2014) and inside and near craters (Campbell et al., 2010; 2009), which also implies that the variation is caused in large part by geometric characteristics, i.e., the surface roughness.

The circular-polarization ratio can vary only due to electric permittivity (Mishchenko and Hovenier, 1995; Virkki et al., 2013).

* Corresponding author. Tel.: +358 503185480.
E-mail address: anne.virkki@helsinki.fi (A. Virkki).

http://dx.doi.org/10.1016/j.icarus.2016.01.011
0019-1035/

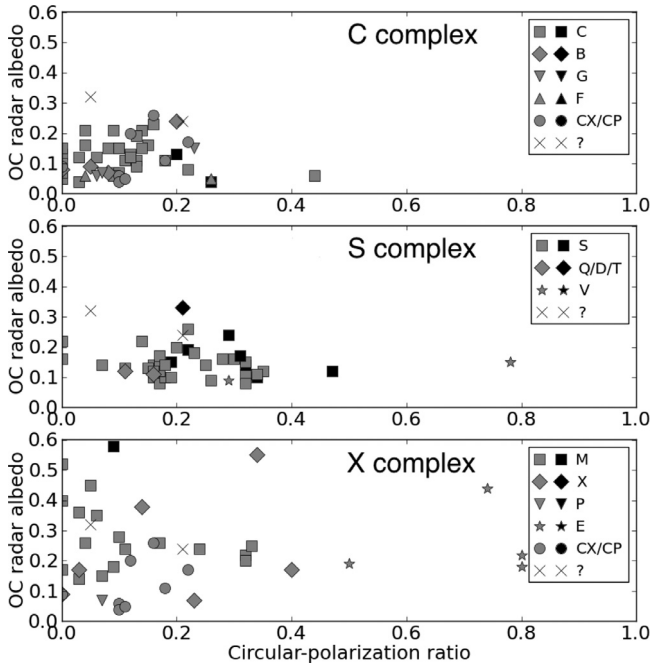

Fig. 1. The radar properties of asteroids of different spectral groups. The gray markers depict main-belt asteroids and the black markers near-Earth asteroids. The Q, D, and T types, with only one representative asteroid in each, and two V types are included with the S type. The types of two asteroids were unknown. For comets, the OC radar albedo is typically less than 0.1 and circular-polarization ratio 0.1–0.6 (Benner et al., 1999; 2002; Brozovic et al., 2009; Busch et al., 2006; de Pater et al., 1994; Harmon et al., 1989; Hudson et al., 2000; 2003; Koyama et al., 2001; Magri et al., 2007a; 1999; 2007b; Mitchell et al., 1996; 1995; Nolan et al., 2005; Ostro et al., 2005; 2004; 1983; 1985; 1999; 2001; 1991; 1989; Shepard et al., 2008a; 2008b; 2010; 2015; Spence et al., 1997; Zaitsev et al., 1997).

However, no robust evidence has been published to explain the variation of the circular-polarization ratio between the different taxonomic types of asteroids, comets, or the local variations in terms of electric permittivity. Therefore, the effect of the electric permittivity on radar scattering plays a significant role in this paper.

The radar albedo is shown to depend on the density of the scattering medium. The near-surface density, which has been discussed in several papers (Garvin et al., 1985; Magri et al., 2001; Ostro et al., 1985; Shepard et al., 2008a; 2010) is thus related to the electromagnetic properties, as the dielectric constant has a positive correlation with density (Rayleigh, 1892). Shepard et al. (2010) suggest that the large range of the values of radar albedo as well as circular-polarization ratio among the M and X type asteroids, and also within specific asteroids, is a result of exaggeration of the irregularities in the shape by the radar reflectivity. Note also that the E- and P-type asteroids may differ in terms of composition substantially compared to the M- and X-type asteroids.

For the icy Galilean Moons Europa, Ganymede, and Callisto, the OC radar albedos are 1.0, 0.6, and 0.3, and the circular-polarization ratios 1.5, 1.4, and 1.2, respectively (Campbell et al., 1978; Ostro et al., 1992). These peculiarly high values have been explained with the coherent-backscattering mechanism (CBM), which can enhance the circular-polarization ratio at backscattering (Black et al., 2001; Hapke, 1990; Mishchenko, 1992; Peters, 1992). The CBM will be treated in this paper as well (the definition of CBM is reviewed in Section 2.4).

Questions, which the current knowledge on radar scattering do not comprehensively answer, are, e.g., what role do different electric permittivities and geometries of the planetary surfaces play in the radar reflectivity and polarization? Is the CBM the only explanation for the high circular-polarization ratios and radar albedos for the icy Galilean Moons? In which cases is the CBM relevant for the radar scattering by asteroid or comet surfaces?

To outline the paper, we give a brief overview of the relevant scattering theory in Section 2. We present the model particles and the selected values for the materials and sizes of the particles in Section 3. We illustrate and discuss the differences in the radar scattering due to different physical parameters in Section 4. And, finally, we summarize and draw conclusions based on the essential results in Section 5.

2. Scattering theory

2.1. Scattering matrix

The intensity and the polarization of an electromagnetic wave can be presented using the Stokes vector $\mathbf{I} = [I, Q, U, V]^T$, where I stands for the intensity, Q and U for the linear polarization, and V for the circular polarization. The ensemble-averaged 4×4 scattering phase matrix $\mathbf{P}(\theta)$ relates the incident and scattered Stokes vectors $\mathbf{I}_{\rm inc}$ and $\mathbf{I}_{\rm sca}$:

$$\mathbf{I}_{\rm sca} = \frac{\sigma_s}{4\pi R^2}\mathbf{P}(\theta)\cdot\mathbf{I}_{\rm inc}, \quad \int_{4\pi}\frac{d\Omega}{4\pi}P_{11} = 1. \tag{1}$$

Here, θ is the scattering angle, i.e., the angle between the incident and scattered wave vectors, R is the distance of the scatterer from the observer, and σ_s is the ensemble-averaged scattering cross section, which describes the total power scattered by a particle in terms of incident power falling on the area σ_s (van de Hulst, 1981).

Similar to σ_s, we can define the absorption cross section as the power incident on the area σ_a that is equal to the power absorbed by a particle, and the extinction cross section as the power incident on the area σ_e that is equal to the power removed from the original beam by scattering and absorption, i.e., $\sigma_s + \sigma_a$. The extinction, scattering, or absorption cross section divided by the projected area, A, gives the extinction, scattering, or absorption efficiencies (q_e, q_s, or q_a), respectively. The ratio of the scattering efficiency to the extinction efficiency is called the single-scattering albedo (ω), which describes the remaining power at each scattering.

2.2. Radar properties

Considering simulations of radar scattering, mainly the backscattering direction ($\theta = 180^\circ$) is relevant. Using radar, the integrated echo power is described using the radar cross section, $\sigma_{\rm back}$. The radar cross section is 4π times the backscattered power per steradian divided by the power incident on a unit area (Bohren and Huffman, 1983).

If the radar cross section is divided by the projected area of the target, the total radar albedo is obtained (i.e., $\sigma_{\rm back}/A = \hat{\sigma}_T$). As well as the radar cross section, the radar albedo can be indicated using a specific polarization state, $\hat{\sigma}_{\rm OC}$ or $\hat{\sigma}_{\rm SC}$. In terms of the scattering-matrix elements, we can define:

$$\begin{aligned}
\sigma_{\rm back} &= \sigma_s P_{11}(180^\circ),\\
\hat{\sigma}_T &= q_s P_{11}(180^\circ),\\
\hat{\sigma}_{\rm SC} &= \frac{\hat{\sigma}_T}{2}\left(1 + \frac{P_{44}(180^\circ)}{P_{11}(180^\circ)}\right),\\
\hat{\sigma}_{\rm OC} &= \frac{\hat{\sigma}_T}{2}\left(1 - \frac{P_{44}(180^\circ)}{P_{11}(180^\circ)}\right),
\end{aligned} \tag{2}$$

The relationship between the OC radar albedo and Fresnel reflectivity R_F is given by Ostro (Ostro et al., 1985) as $\hat{\sigma}_{\rm OC} = gR_F$, where the 'gain factor' g depends on the target's angular scattering

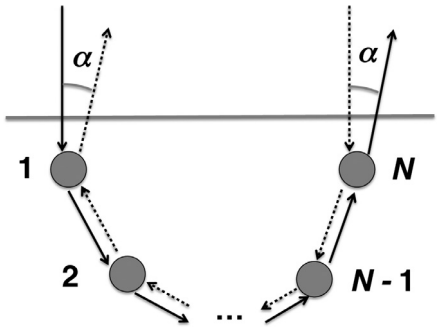

Fig. 2. The interference effect of the coherent-backscattering mechanism. The phase angle $\alpha = 180^\circ - \theta$. The numbers 1, 2, ...$N$ depict the order of scattering.

law, shape, and orientation for large, absorbing objects. The Fresnel reflectivity for a normal incidence is

$$R_F = \left| \frac{m-1}{m+1} \right|^2, \tag{3}$$

where m is the complex refractive index.

The circular-polarization ratio μ_C is the ratio of the echo power in the SC polarization state to that in the OC polarization state. In terms of the elements of the scattering matrix (see, e.g., Bohren and Huffman, 1983), μ_C can be presented in the backscattering direction for ensembles of particles in random orientations:

$$\mu_C(180^\circ) = \frac{\sigma_{\text{back,SC}}}{\sigma_{\text{back,OC}}} = \frac{\hat{\sigma}_{\text{SC}}}{\hat{\sigma}_{\text{OC}}} = \frac{P_{11}(180^\circ) + P_{44}(180^\circ)}{P_{11}(180^\circ) - P_{44}(180^\circ)}. \tag{4}$$

For a spherical particle or a semi-infinite half-space of optically isotropic and homogeneous material bounded by a plane interface, $\mu_C(180^\circ) = 0$.

2.3. Linear-polarization ratio

The linear-polarization ratio is theoretically related to the circular-polarization ratio at backscattering for ensembles of particles and their mirror particles (van de Hulst, 1981). Using a linearly polarized incident wave $\mathbf{I}_{\text{inc}} = (1, \pm 1, 0, 0)$, the linear-polarization ratio can be defined in the backscattering direction as

$$\mu_L(180^\circ) = \frac{P_{11}(180^\circ) - P_{22}(180^\circ)}{P_{11}(180^\circ) + P_{22}(180^\circ)}, \tag{5}$$

which is related to the circular-polarization ratio so that at backscattering $\mu_L = \mu_C/(2 + \mu_C)$ (Mishchenko and Hovenier, 1995). For ground-based observations, circular polarization is a safer choice for the signal than linear polarization, because the charged small particles in the atmosphere may cause rotation of the polarization.

2.4. The coherent-backscattering mechanism

Multiple scattering by a medium with numerous scatterers is the sum of two parts: the incoherent and coherent scattering. The incoherent part refers to the diffuse radiation by the first-order scattering and the so-called ladder terms of the Bethe–Salpeter equation (Tsang et al., 1985). The coherent part refers to the interference of conjugate pairs of waves scattered along two reversed trajectories (see Fig. 2). In the exact backscattering direction, the interference is always constructive, which causes a backscattering peak. Therefore, the enhancement mechanism is called the coherent-backscattering mechanism (CBM). The coherent part is the sum of the cyclical terms of the Bethe–Salpeter equation. The CBM is more relevant for wavelength-scale scatterers than for scatterers in the geometric-optics regime.

The coherent backscattering term, or the cyclical component at backscattering (superscript C), can be theoretically derived from the ladder components (superscript L) (Mishchenko, 1996):

$$\begin{aligned}
P_{11}^C &= \frac{\sigma_s^L}{2\sigma_s^C}(P_{11}^L + P_{22}^L - P_{33}^L + P_{44}^L),\\
P_{22}^C &= \frac{\sigma_s^L}{2\sigma_s^C}(P_{11}^L + P_{22}^L + P_{33}^L - P_{44}^L),\\
P_{33}^C &= \frac{\sigma_s^L}{2\sigma_s^C}(-P_{11}^L + P_{22}^L + P_{33}^L + P_{44}^L),\\
P_{44}^C &= \frac{\sigma_s^L}{2\sigma_s^C}(P_{11}^L - P_{22}^L + P_{33}^L + P_{44}^L).
\end{aligned} \tag{6}$$

If only the incoherent (radiative transfer, superscript "RT") part, and the first-order-scattering (superscript "(1)") part are available, the ladder part is computed so that

$$\sigma_s^L \mathbf{P}^L = \sigma_s^{\text{RT}} \mathbf{P}^{\text{RT}} - \sigma_s^{(1)} \mathbf{P}^{(1)} \tag{7}$$

Using these equations, $\hat{\sigma}_{\text{SC}}$ and $\hat{\sigma}_{\text{OC}}$ including both the radiative-transfer and the cyclical parts are therefore

$$\begin{aligned}
\hat{\sigma}_{\text{SC}} &= \frac{q_s^{\text{RT}}}{2}\left(P_{11}^{\text{RT}} + R_{11} + P_{44}^{\text{RT}} + R_{44}\right), \quad \text{and}\\
\hat{\sigma}_{\text{OC}} &= \frac{q_s^{\text{RT}}}{2}\left(P_{11}^{\text{RT}} + R_{11} - P_{44}^{\text{RT}} - R_{44}\right), \quad \text{where}\\
R_{11} &= \frac{1}{2}\left[P_{11}^{\text{RT}} + P_{22}^{\text{RT}} - P_{33}^{\text{RT}} + P_{44}^{\text{RT}} - \left(P_{11}^{(1)} + P_{22}^{(1)} - P_{33}^{(1)} + P_{44}^{(1)}\right)\frac{\sigma_s^{(1)}}{\sigma_s^{\text{RT}}}\right],\\
R_{44} &= \frac{1}{2}\left[P_{11}^{\text{RT}} - P_{22}^{\text{RT}} + P_{33}^{\text{RT}} + P_{44}^{\text{RT}} - \left(P_{11}^{(1)} - P_{22}^{(1)} + P_{33}^{(1)} + P_{44}^{(1)}\right)\frac{\sigma_s^{(1)}}{\sigma_s^{\text{RT}}}\right].
\end{aligned} \tag{8}$$

3. The computational methods

For the modeling, we use Siris, a code developed by Muinonen et al. (2009) for simulating light scattering by Gaussian-random-sphere (GRS) particles (Muinonen et al., 1996) that are large compared to the wavelength. The user is able to define the geometry, size, and material of the particles. The GRS particle is described in spherical coordinates by the spherical-harmonics series as shown, e.g., in Muinonen et al. (1996, 2009); Peltoniemi et al. (1989); Virkki and Muinonen (2015b). We omit the mathematical formulation here, as only relatively spherical GRS particles will be used. The specific shape of the host particle plays here a minor role.

In addition to the ray-optics part, the algorithm includes diffuse scattering. The diffuse medium can be considered as wavelength-scale particles on the surface of a large host particle or inside it (a diffuse external or internal medium, respectively). Numerically, the diffuse medium is treated as a user-defined scattering matrix, which is an average of numerous scattering matrices of single diffuse scatterers (see Section 3.2 for the detailed description of the averaging).

As the diffuse scatterers, we utilize three different irregular geometries (particles A, B, and C) that have been originally laboratory-characterized to simulate light scattering by realistic atmospheric dust particles (Lindqvist et al., 2014). The surface topography has been determined from a stereo pair of scanning-electron-microscope images acquired from different tilt angles. As we can see in Fig. 3, which shows the dust particles, although the shape characterization was carried out for micrometer-scale particles, the shapes of decimeter-to-meter-scale boulders collected on the Moon during the Apollo program closely resemble those of the dust particles.

An orientation-averaged scattering matrix is computed for each scatterer, A, B, and C, using the discrete-dipole approximation algorithm ADDA (Draine and Flatau, 1994; Yurkin and Hoekstra, 2011).

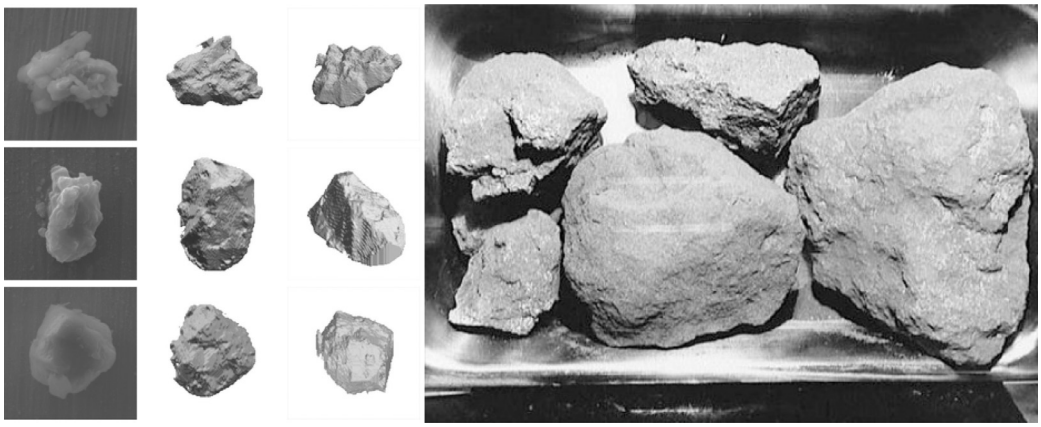

Fig. 3. On the left: The scanning-electron-microscope images and the shape models of three dust particles (Lindqvist et al., 2014). In the text, the geometries of the dust particles are referred to as particle A (on the top), B (in the middle), and C (on the bottom). On the right: Boulders of rock collected from the Moon (photo credit: NASA).

Table 1
The selected values of mean free path (l) and optical thickness (τ_s) for $\lambda = 12.6$ cm. The optical thickness corresponds to the mean free paths and a mean layer thickness of 40 cm (see Eq. 9). The bottom line lists the geometric, two-dimensionally projected surface density of the layer of diffuse external medium for each optical thickness.

l (m)	0.13	0.38	0.63	1.26	2.52	5.04	10.08
l (λ)	1	3	5	10	20	40	80
τ_s	3.08	1.05	0.63	0.32	0.16	0.08	0.04
κ_s (%)	95	65	47	27	15	8	4

In the discrete-dipole approximation, the scatterer is divided into small enough voxels that each can be treated as an electric dipole. The number of dipoles per wavelength should be larger than 10 times the refractive index (here, 15 is used as minimum). Also, we used filtered-coupled-dispersion mode for polarizability prescription and interaction term instead of the default point dipoles and lattice dispersion relation when the real part of the refractive index exceeded 2.

The default orientation-averaging algorithm of the ADDA was considered overly time-consuming for the largest particles. In order to reduce the required CPU time, we used a cubature method by Penttilä and Lumme (2011). This decreased the number of orientations from 7200 to 2592 and the CPU time by 70–80% without significant loss in the accuracy.

The diffuse external medium on the host particle can be physically considered as regolith pebbles or boulders on a planetary surface, e.g., an asteroid or a Moon. The quantity of surface material varies greatly depending on the object, but also locally, as images of asteroids, e.g., (25143) Itokawa show (Saito et al., 2006).

The number density is described using the optical thickness (τ_s) for the diffuse external medium, and using the mean free path (l) for the diffuse internal scatterers. Physically, the mean free path describes the mean distance between two scattering events. For both cases, the algorithm also requires the single-scattering albedo.

The scalar extinction coefficient, k_0, can be used for describing both τ_s and l:

$$\tau_s = \int_0^s k_0 ds = k_0 s = s/l, \quad l = \frac{1}{k_0}, \tag{9}$$

where, using the number and volume densities n_0 and v_0, respectively,

$$k_0 = n_0 q_e \pi a^2 = \frac{3 v_0 q_e}{4a}, \quad n_0 = \frac{3 v_0}{4\pi a^3}. \tag{10}$$

The selected values are listed in Table 1. Extinction is assumed to be exponential. The geometric, two-dimensionally projected surface density of the layer of diffuse external medium is

$$\kappa_s = (1 - e^{-\tau_s}) \times 100\% \tag{11}$$

The values were selected considering that the mean free path should exceed the wavelength and also, substantially, the mean size of the scatterers as the near-field effects between the particles are not accounted for in the algorithm based on the Monte Carlo ray-tracing technique. According to Virkki and Muinonen (2015a), the near-field effects can have a significant effect on the SC radar albedo. Therefore, the results, which were computed using the first values in the list (e.g., $l = 0.13$ m), are included as points of high interest but should be considered with caution. The mean layer thickness ($s = 0.4$ m) was selected based on the scatterer sizes (see Section 3.2).

By default, Siris computes the scattering matrix including only the radiative transfer part, that is, the single scattering and ladder terms. Therefore, in order to include the cyclical part described in Section 2.4, we carry out additional corrective computations using Eq. (6) when treating wavelength-scale scatterers. This gives an approximation of the maximum enhancement caused by the CBM.

It has been recently shown by Muinonen et al. (2012) that the radiative-transfer coherent-backscattering modeling is capable of reproducing exact electromagnetic results for loosely packed finite systems of scatterers. This speaks for the relevance of the present modeling of diffusely scattering external and internal media.

In addition, the output always includes numerical noise as typical for a Monte Carlo ray-tracing method. Therefore, we optimize the CPU time by using enough (6–10 million) rays to reach an acceptable accuracy for the scattering matrix, and carry out a smoothing spline fit (Hastie and Tibshirani, 1990) to the required scattering-matrix elements before computing the CBM corrections and the radar parameters.

For example, if we model the scattering-matrix elements by the relation $Y_i = \eta(\theta_i)$, where θ_i is one scattering angle between 90° and 180° with a resolution of 1°, the smoothing spline estimate $\hat{\eta}$ of the function η is defined to be the minimizer of

$$f(\hat{\eta}, \hat{\beta}) = \sum_{i=1}^{91} (Y_i - \hat{\eta}(\theta_i))^2 + \hat{\beta} \int_{90^\circ}^{180^\circ} \hat{\eta}''(\theta)^2 d\theta. \tag{12}$$

Above, $\hat{\beta}$ is a smoothing parameter that controls the fidelity between the data and roughness of the function estimate. Here, we use values of $\hat{\beta}$ case-by-case from 0.05 to 0.1. The values have been chosen empirically so that the fit does not excessively try to follow the noise (too small a value) nor to smooth down the possible curvature (too high a value).

Table 2
The electric permittivities and refractive indices of the materials. The second column lists the electric permittivity of the diffuse scatterers, the third column lists the refractive index of the host particle, and the fourth column lists the refractive index of the scatterer relative to the medium, i.e., in the case of the internal scatterers (the last four lines), $m_r = m_s/m_p$. The fifth column lists the average single-scattering albedo for each material. The porosity of porous (or powdered) ice is 52%, estimated using the Rayleigh mixing formula (Rayleigh, 1892), and FGR refers to fine-grained regolith (here, powder density c. 1 g/cm^3, as given in Campbell and Ulrichs, 1969).

Material	ϵ_s	m_p	m_r	ω
Solid ice	$3.17 + 0.004$i	$1.78 + 0.001$i	$1.78 + 0.001$i	0.99
Rock 1	$4.67 + 0.022$i	$2.16 + 0.005$i	$2.16 + 0.005$i	0.94
Rock 2	$6.45 + 0.051$i	$2.54 + 0.01$i	$2.54 + 0.01$i	0.90
Voids in solid ice	$1.0 + 0$i	$1.78 + 0.001$i	$0.56 + 0$i	1.0
Ice in porous ice	$3.17 + 0.004$i	$1.36 + 0.001$i	$1.31 + 0.0007$i	0.99
Rock 2 in solid ice	$6.45 + 0.051$i	$1.78 + 0.001$i	$1.43 + 0.006$i	0.93
Rock 2 in FGR	$6.45 + 0.051$i	$1.375 + 0.001$i	$1.85 + 0.007$i	0.92

3.1. Materials

For asteroids, relevant materials to study are silicate-, carbon-, and basalt-rich materials. We describe rocky materials referring to common silicate-rich rock types such as anorthosite, olivine, and basalt. Materials with high metal content are numerically problematic due to their magnetic properties that are unknown at microwave frequencies and their extremely high absorption. Also, ice will be discussed as a relevant material especially for the Galilean Moon Europa.

Table 2 lists the materials that were selected for the study as well as their scattering properties. The first section includes values of electric permittivity of the scatterers (ϵ_r), refractive index of the medium (m_m), relative refractive index of the scatterers (m_r), and the single-scattering albedo (ω) selected for diffuse external scatterers: Ice and two types of rocky material. The first type of rock ("rock 1") refers to fractured or porous silicates with negligible metal content. The second type ("rock 2") refers to solid silicate rock with minor metal content.

The values have been selected using the microwave electric permittivities (at frequency of 450 MHz) reported by Campbell and Ulrichs (1969) as guidelines. For example, for olivine and anorthosite, refractive indices of 2.49 + 0.013i and 2.61 + 0.0096i can be deduced from the reported electric permittivities. For basalts, the refractive index varies from 2.37 + 0.012i to 3.10 + 0.145i. For nearly all of the powders that they measured, it was concluded that with a density of 1.0 g/cm^3, the electric permittivity can be approximated to 2.0 (±10%). Measurements of electric properties of meteorites support the applicability of the values (E. Heggy, personal communication).

For pure, solid water ice, the complex refractive index is from $1.76 + 0$i to $1.77 + 0.0001$i, slightly depending on the literature source as Warren shows in Warren (2008). In space environment, however, the ice is likely to host impurities that slightly increase the real as well as the imaginary part of the refractive index. The ice treated here (solid as well as porous) is not considered completely pure water ice but is assumed to include microscale impurities such as dust or other non-volatiles, which increases the real and imaginary parts of the refractive index slightly. Therefore, we use, by default, $m = 1.78 + 0.001$i for solid ice, and use non-absorbing ice ($m = 1.76 + 0$i) only for demonstrative reasons in Section 4.3.

In the second section, the selected values for the diffuse internal scatterers are listed: Macroporosity or void inclusions in solid ice, solid ice in porous ice (porosity of 52%), rock 2 in ice, and rock 2 in dust-like, fine-grained regolith (abbreviated below as FGR). The refractive indices for solid ice and rock 2 are the same as for the diffuse external medium. In addition, FGR is introduced with, here, $m_p = 1.375 + 0.001$i (powder density of approximately 1 g/cm^3) and porous ice with $m_p = 1.36 + 0.001$i. Note that the relative refractive index of rock 2 in FGR could also apply to rock inside porous ice.

The radar observations can also be utilized to constrain the realistic range of refractive indices of certain types of planetary targets. Estimate of the refractive index is important not only with regard to modeling, but can help to evaluate the chemical (e.g., the content of metal) and structural composition (e.g., the density or the porosity) of the surface, which are related to the refractive index. Consequently, implications of the formation of the planetary body can be acquired.

Assuming that Eq. (3) applies and $\mathrm{Im}(m) \ll \mathrm{Re}(m)$, the mean OC radar albedo for the C-complex asteroids, $\hat{\sigma}_{\mathrm{OC}} \approx 0.12 \pm 0.05$, constrains the real part of the refractive indices to extend from 1.7 to 2.4. For an average S-type asteroid $\hat{\sigma}_{\mathrm{OC}} \approx 0.15 \pm 0.04$, which allows a range of $\mathrm{Re}(m)$ to extend from 2.0 to 2.6.

For comets, the observed OC radar albedos are relatively low, which suggests low refractive indices ($\mathrm{Re}(m) < 2$). However, considering the surface as ice is unrealistic: Spectral measurements by Rosetta spacecraft of the comet 67P/Churyumov–Gerasimenko suggest crustal composition of polyaromatic organic solids mixed with sulfides and iron-nickel alloys. No ice-rich patches were observed (Capaccioni et al., 2015).

For X-complex asteroids with high metal content, $m = 2.9 + 0.02$i or higher values for both the real and the imaginary parts could be realistic. If the iron content is very high, also the magnetic permeability can become prominent (much greater than 1), and thus, affect the refractive index. However, as was evident in Fig. 1, the X complex shows the widest range of values in $\hat{\sigma}_{\mathrm{OC}}$, which implies a wide spread in the composition as well. Therefore, all X-complex asteroid are not likely to have a high metal content, although their spectra measured on optical and infrared wavelengths may be similar.

3.2. Sizes

The size relative to the wavelength is described using the size parameter:

$$x = \frac{2\pi a}{\lambda}, \tag{13}$$

where a is the mean radius. For irregular particles, we use the volume-equivalent-sphere size parameter.

The size-averaged scattering phase matrix $\mathbf{P}(\theta)$ is computed by weighting each particle using the size distribution, $n(x)$, and the scattering cross section, σ_s:

$$\mathbf{P}(\theta) = \langle \mathbf{P}(\theta, x) \rangle = \frac{\sum_{x=0.5}^{\max(x)} \mathbf{P}(\theta, x) n(x) \sigma_s(x)}{\sum_{x=0.5}^{\max(x)} n(x) \sigma_s(x)}. \tag{14}$$

For the extinction and scattering efficiencies, the weighted averages are, respectively:

$$\langle q_e \rangle = \frac{\sum_{x=0.5}^{\max(x)} \sigma_e(x) n(x)}{\sum_{x=0.5}^{\max(x)} A(x) n(x)}, \quad \langle q_s \rangle = \frac{\sum_{x=0.5}^{\max(x)} \sigma_s(x) n(x)}{\sum_{x=0.5}^{\max(x)} A(x) n(x)}. \tag{15}$$

The average single-scattering albedo is therefore $\langle \omega \rangle = \langle q_s \rangle / \langle q_e \rangle$.

Based on the studies by Shoemaker and Morris (1968); Tatsuhiro Michikami et al. (2008), the size distribution of regolith particles can be approximated using the power-law size distribution $n(a) \propto a^{-3}$. The effect of the power-law index is not very significant, i.e., a 10 % change in the power-law index causes less than 10 % change in the average scattering-matrix elements.

For wavelength-scale scatterers, we only compute the scattering for particles, for which the weight on the diffuse-medium-scattering matrix is larger than 3 % of the maximum and $x \leq 20$.

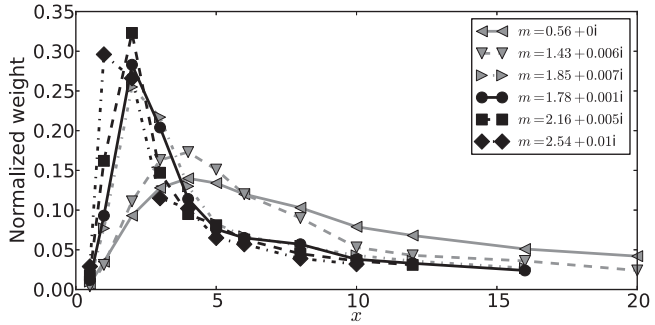

Fig. 4. The normalized weight as a function of size using different refractive indices. Using $\lambda = 12.6$ cm, the mean radius of a scatterer $a \approx 2x$ cm.

The lower limit is held at $x = 0.5$ for all the scatterers, but due to the limitation, the upper limit varies case-by-case. An exception is made for the shortest mean free path ($l = 0.13$ m), for which $x \leq 10$.

The normalized weights of the utilized refractive indices are illustrated in Fig. 4 using normalization:

$$\sum_{x=0.5}^{\max(x)} n(x)\sigma_s(x) = 1$$

By default, we use 252 m as the mean diameter of a host particle, that is, the asteroid, and $\lambda = 12.6$ cm (S band), in which case the minimum absolute mean radius $a_{\min} = 1$ cm and the maximum mean radius $a_{\max} = 40$ cm. From Fig. 4 we can therefore deduce that the most effective mean scatterer diameter in terms of the S-band radar is only 5–8 cm when $\mathrm{Re}(m) > 1.5$. When $\mathrm{Re}(m) < 1.5$, the particles with a mean diameter of 16 cm are the most effective contributors.

If the wavelength were 3.5 cm, $a_{\min} = 0.3$ cm and $a_{\max} = 11$ cm for the same range of size parameters, and the most effective mean diameters were 1–4 cm. Or optionally, if the wavelength were 70 cm, we would have $a_{\min} = 6$ cm and $a_{\max} = 222$ cm and the most effective mean diameters were 20–90 cm.

For comparison, we also utilize another set of super-wavelength-scale scatterers, i.e., boulders, for which the scattering properties were computed by Virkki and Muinonen (2015b). Essentially, for the present study, ensemble-averaged scattering phase matrices are computed for GRS particles (see Section 3), which are 0.8–3 meters in radius (using $\lambda = 12.6$ cm) and do not include diffuse scattering in any form. The standard deviation of the radius is 0.1 for 50% of the GRS particles and 0.2 for the second 50%. Similar to the wavelength-scale scatterers, power-law size distribution with a power-law index of -3 has been utilized for computing the ensemble-averaged scattering matrix.

4. Results and discussion

First, we discuss the geometric effects by comparing irregular and spherical scatterers. The differences due to the geometry are demonstrated first in terms of single scattering and then in terms of multiple scattering. Second, we discuss how the number density of the irregular external or internal scatterers or the CBM affect the radar observables ($\hat{\sigma}_{\mathrm{SC}}$, $\hat{\sigma}_{\mathrm{OC}}$, and μ_C) when different materials are used. Third, we compare the multiple scattering by pebbles (wavelength-scale scatterers) to boulders (scatterer size much larger than the wavelength) in order to discuss the effect of the size distribution and absorption. And last, we discuss the simulation results in terms of planetary surfaces.

4.1. Single scattering and the effect of the geometry

Figs. 5 and 6 illustrate the average scattering-phase-matrix elements, which are utilized as the input data for the diffuse external and internal media, respectively. Here, the scattering-phase-matrix elements of irregular scatterers and their average are compared to those of perfectly spherical scatterers, when only single scattering is treated. As is well known, the polarization elements P_{22} and P_{44} are the most sensitive to the scatterer shape at backscattering. Especially for ice particles, the scattering-phase-matrix elements reveal distinct differences in the backscattering direction between spherical and irregular scatterers, which could suggest a strong enhancement in the backscattering direction when applied to the multiple-scattering scenario.

Fig. 7 illustrates the radar observables (including the CBM correction) as a function of the number density of the scatterers (as explained in detail in Section 3). The computations carried out using spherical particles compared to irregular particles of ice and rock reveal a remarkable difference. Indeed, while the values of μ_C and $\hat{\sigma}_{\mathrm{OC}}$ computed using rock 2 can double when using spherical scatterers instead of irregular ones, for ice, they can triple. As for $\hat{\sigma}_{\mathrm{SC}}$, the geometry as well as the electric permittivity play a smaller role. In the case of internal scatterers (Fig. 8), the specific shape plays a secondary role for the OC radar albedo as well.

What causes the dramatic difference between the geometries in the external case, and between the external and internal cases? The major part of $\hat{\sigma}_{\mathrm{OC}}$ arises from the first-order backscattering independent of the geometry of the scatterers (Virkki and Muinonen, 2015a) (see Fig. 9). Therefore, what we see in the single-scattering features is reflected in the multiple-scattering features: a backscattering peak of a spherical scatterer causes extra enhancement compared to an irregular scatterer. As for $\hat{\sigma}_{\mathrm{SC}}$, already the first-order backscattering may contribute, but only if the scatterers are irregular. In the case of spherical scatterers, $\hat{\sigma}_{\mathrm{SC}}$ arises only from the second and higher orders of scattering.

In addition to the geometry, the path of the radiation and the material affect the echo. As Figs. 5 and 6 show, the radiation tends to scatter more forward than backward. As for the external scatterers, the forward-scattered radiation in the first-order scattering is likely to be absorbed into the host particle. The most likely contribution to the echo after the first-order backscattering is thus two scatterings in angles of approximately 90°, commonly known as double bounce. In between the scatterings, a reflection from the surface of the host particle is also possible. As for the internal scatterers, more forward-scattering takes place, but the signal is also more sensitive to the absorption of the material. Therefore, e.g., void inclusions enhance $\hat{\sigma}_{\mathrm{SC}}$ more than the rock inclusions in ice. In addition, small part of the signal power is reduced on each pass of the surface of the host particle in Fresnel reflections and refractions.

4.2. The number density of scatterers

Let us begin here with the diffuse external medium. Fig. 10 illustrates the effect of the optical thickness on $\hat{\sigma}_{\mathrm{SC}}$, $\hat{\sigma}_{\mathrm{OC}}$, and μ_C using three different materials: solid ice, and two different rocks (see Section 3.1 for the details). As well, the effect of CBM is presented compared to the radiative transfer solution. Note that $\hat{\sigma}_{\mathrm{OC}}$ for $\tau_s = 0$ is not a result of simulations but computed using Eq. (3). Similarly, $\hat{\sigma}_{\mathrm{SC}}$ and, consequently, μ_C for $\tau_s = 0$ are assumed to be 0.

Fig. 11 shows the scattering properties for the diffuse internal scatterers, which mimic macroporosity or void inclusions in solid ice, solid ice in porous/powdered ice (porosity of 52%), rock 2 in ice, and rock 2 in dust-like, fine-grained regolith (FGR). The CBM is included but not compared to the radiative-transfer solution for illustration clarity. Similar to the diffuse external medium, the CBM

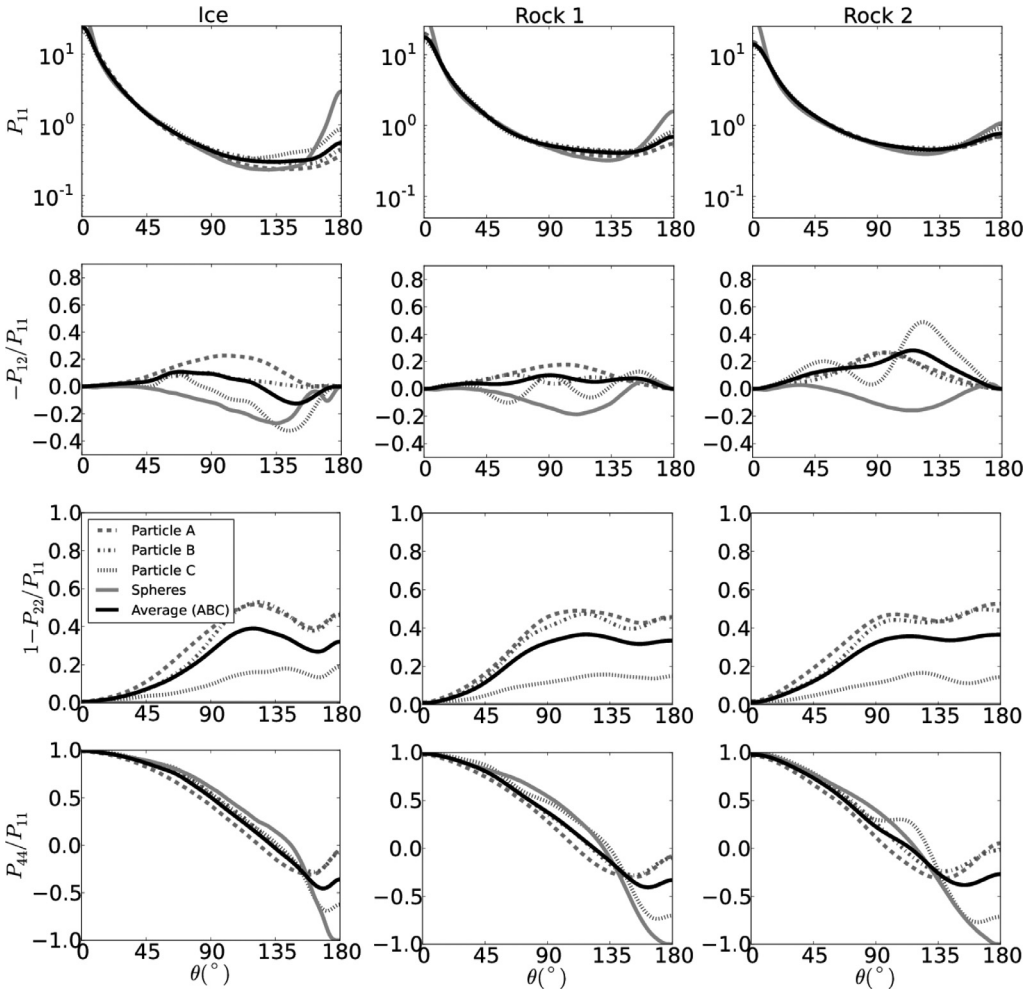

Fig. 5. From the top: P_{11}, $-P_{12}/P_{11}$, $1-P_{22}/P_{11}$, and P_{44}/P_{11} as a function of the scattering angle when the scatterers are composed of ice (the first column), rock 1 (the second column), or rock 2 (the third column). The dashed, dotted, and dash-dotted lines depict the three different irregular geometries and the black line the average of the three. The gray solid line depicts spheres with the same size distribution.

increases the SC and OC radar albedos. Therefore, these values can be considered as upper bounds.

We can make several interesting interpretations from Figs. 10 and 11. First, a larger number density of surface scatterers increases, and only increases $\hat{\sigma}_{\mathrm{OC}}$, i.e., the radar reflectivity is not only a function of metal content (here, the electric permittivity) or the surface density but also the surface roughness. Therefore, both $\hat{\sigma}_{\mathrm{OC}}$ as well as μ_C can be expected to be greater for asteroids with wavelength-scale scatterers on the surface than for asteroids in the same taxonomic class and comparable near-surface packing density without wavelength-scale scatterers.

Second, the CBM increases all radar observables, as expected. The enhancement depends on the number density of multiple scattering but not the electric permittivity, and it is more substantial for $\hat{\sigma}_{\mathrm{SC}}$ than for $\hat{\sigma}_{\mathrm{OC}}$.

Third, for the internal scatterers, the echo power depends substantially on the mean free path, and also, the absorption of the scatterers. If the mean free path is small enough, i.e., comparable to one wavelength, solid ice inclusions in ice powder with porosity of 52% reproduce μ_C as high as 2.0. Although short mean free paths should be considered with caution in ray-tracing models, the result is reasonable: for scatterers with low absorption in a medium with low absorption as well, the circular-polarization can be effectively enhanced by the multiple scattering as we discussed in the previous section.

Rock scatterers in ice produce fainter SC and OC echoes than void inclusions in ice (or solid ice inclusions in ice powder), likely due to their higher absorption. The values of μ_C are comparable to voids inside solid ice due to the single-scattering properties of the void inclusions: although there is no absorption, there is also no backscattering peak for the first-order-scattering contribution, which exists for the rock scatterers.

The strongest SC and OC echoes in our internal-scatterer model is reproduced by rock 2 in FGR (or powdered/porous ice) with substantial polarization ratios as well. This supports that also rocks below the surface can produce prominent radar echoes and circular-polarization ratios even when there are no rocks on the surface, however, depending on the absorption of the host material. Note the fact that although the theoretical minimum of $\hat{\sigma}_{\mathrm{OC}}$ is as low as 0.025, the mean free path of 10 m is enough to increase it to 0.11. Similar to ice, the relative refractive index of rock 2 in FGR is such that a backscattering enhancement is prominent in single scattering, which could partly explain the high values of $\hat{\sigma}_{\mathrm{OC}}$.

The results contradict, in part, the results by Black et al. (2001), in which the SC and OC radar reflectivities, as well as μ_C, were modeled using spherical solid-ice scatterers in porous/powdered ice, void scatterers in solid ice, and rock scatterers in solid ice. Values observed for the Galilean Moons were to be reproduced by searching for the best fit for various physical parameters. The

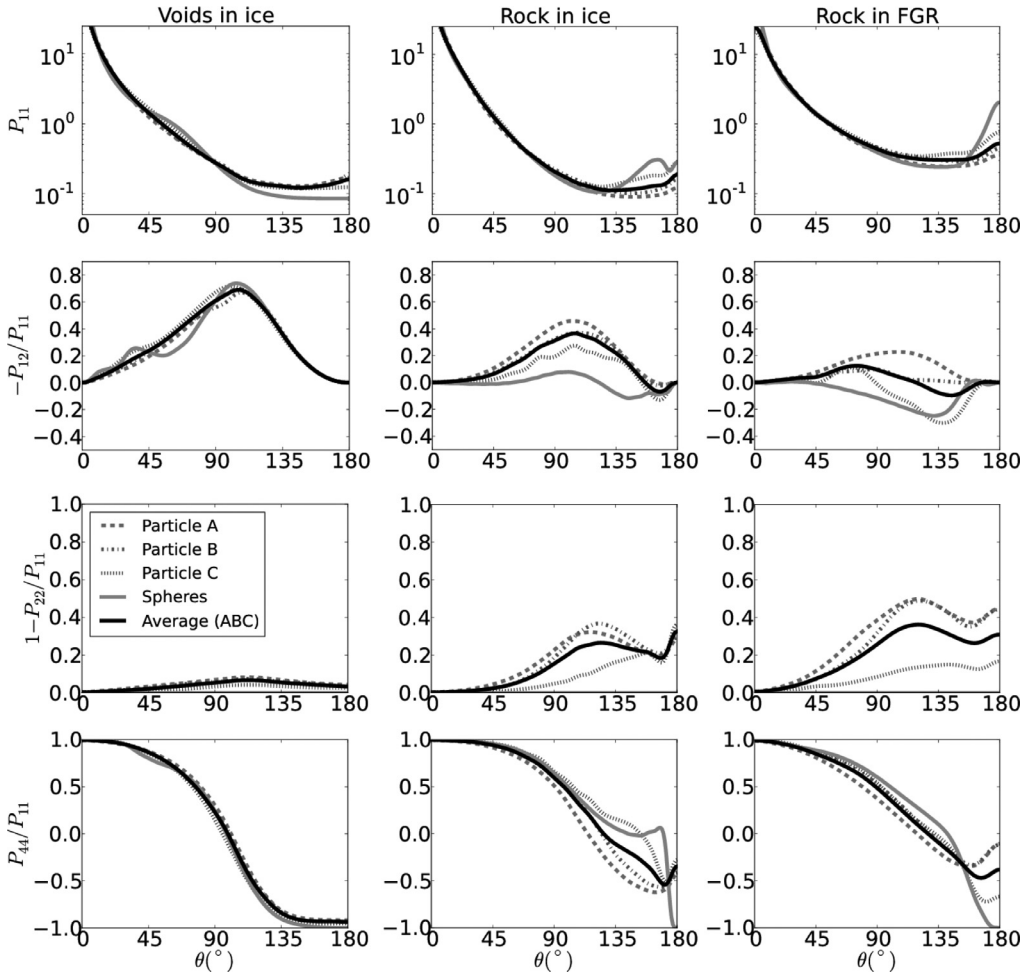

Fig. 6. From the top: P_{11}, $-P_{12}/P_{11}$, $1-P_{22}/P_{11}$, and P_{44}/P_{11} as a function of the scattering angle, when the scatterers are void inclusions in ice (the first column), solid rock (2) in ice (the second column), and solid rock (2) in powdered rock (the third column). The dashed, dotted, and dash-dotted lines depict the three different stereogrammetric geometries and the black line the average of the three. The gray solid line depicts spheres with the same size distribution.

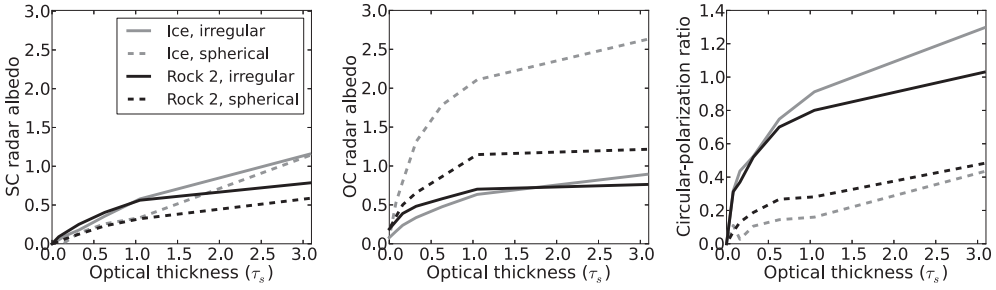

Fig. 7. The SC and OC radar albedo and the circular-polarization ratio as a function of the optical thickness of the diffuse external medium, which is composed of the irregular or spherical particles. Here, only ice (gray) and rock 2 (black) are compared for clarity. CBM is included.

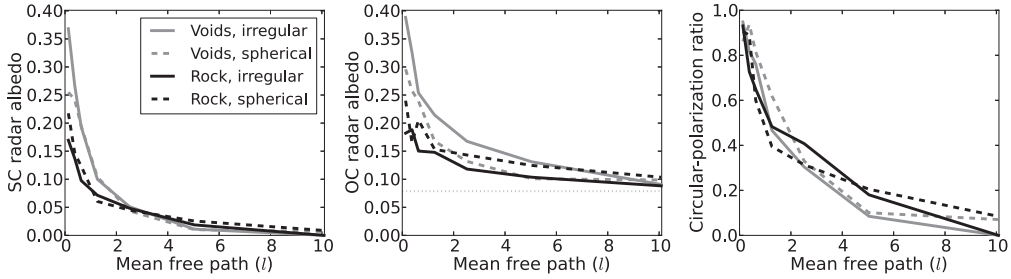

Fig. 8. The SC and OC radar albedo and the circular-polarization ratio as a function of the mean free path in meters when using a diffuse internal medium that is composed of irregular or spherical particles. Here, void inclusions (gray) and rock 2 (black) inside ice are compared. CBM is included.

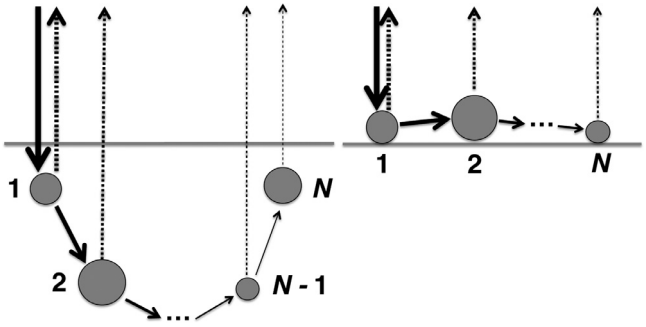

Fig. 9. The contributions of different orders of scattering to the radar echo in a diffuse internal medium (on the left) or in a diffuse external medium (on the right). The width of the arrow depicts the power of the signal and the number depicts the order of scattering. Note that the Fresnel reflections and refractions are omitted here for the clarity of the illustrations. Nevertheless, on each pass of the plane interface, a small part of the remaining signal energy is lost.

results suggested that only void inclusions in ice and solid ice scatterers in porous/powdered ice could reproduce the high SC and OC radar reflectivities.

Their rock scatterer model, which was excluded from the possible solutions, had a relative refractive index $1.58 + 0.02$i, i.e., very high absorption, and the mean free paths in their model were as small as 0.07 m, i.e., in or below wavelength-scale. Also, they did not test rock scatterers inside porous/powdered ice, while in our model, rock-2 scatterers in powdered rock, or ice, return systematically higher values of $\hat{\sigma}_{\mathrm{OC}}$ and μ_C than scatterers inside solid ice. This implies that excluding rock scatterers from the explanation for the high radar reflectivities and circular-polarization ratios of the Galilean Moons should be considered with caution.

The rate of change in terms of the number density of scatterers can be explained with the absorption of the materials. High absorption of the scatterers and the host medium can have a decreasing effect on the radar observables as has been discussed also in Virkki and Muinonen (2015b).

4.3. Large boulders

The effect of absorption becomes even more prominent, when the scatterers are large compared to the wavelength. In Fig. 12, the simulated radar observables are illustrated for boulders, which are 0.8–3 m in radius (see Section 3.2). Note that here, the CBM is not relevant, as all scattering is ray optics. Instead, the absorption plays more significant part compared to the wavelength-scale scatterers as a larger part of the incident radiation is absorbed by the diffuse scatterers. For comparison, we also include ice boulders without absorption, using $m = 1.76 + 0$i ($\omega = 1.0$), depicted "ice 1". For other materials, ω for ice (here, "ice 2"), rock 1, and rock 2 are 0.61, 0.27, and 0.25, respectively. The mean layer depth is 3 m.

We can see the same scattering features that we saw for the wavelength-scale scatterers: as the absorption increases, the rate of change of the radar observables as a function of the number density of scatterers decreases. In contrast to the wavelength-scale scatterers, for rock 1 and 2, the OC radar albedo even slightly decreases, as the number density of more absorbing boulders increases. As was shown in Virkki and Muinonen (2015b), if $\mathrm{Im}(m) \geq 0.005$, diameter of 3 m is enough to absorb all energy, if $\mathrm{Im}(m) \geq 0.01$, diameter of 2 m is enough, and so on. Therefore the scattering matrices of these materials are relatively similar on the selected size range and only small differences are visible due to different single-scattering albedos.

4.4. Interpretations in terms of planetary surfaces

Next, we compare the simulations to the observed values, beginning with the asteroid taxonomy discussed in Section 1. Fig. 13 depicts the modeled radar observables in the $\hat{\sigma}_{\mathrm{OC}}$-$\mu_C$ space, which enables more convenient comparison with the observed data in Fig. 1. Increasing the number density of scatterers moves the position of the marker diagonally from lower left to upper right.

The range of modeled values is mainly comparable to the observed data, excluding the cases using the largest optical depths. For wavelength-scale scatterers, the minimum modeled values of $\hat{\sigma}_{\mathrm{OC}}$ are obtained using host particles (e.g., asteroids) without diffuse scatterers. The minimum observed values of $\hat{\sigma}_{\mathrm{OC}}$ are

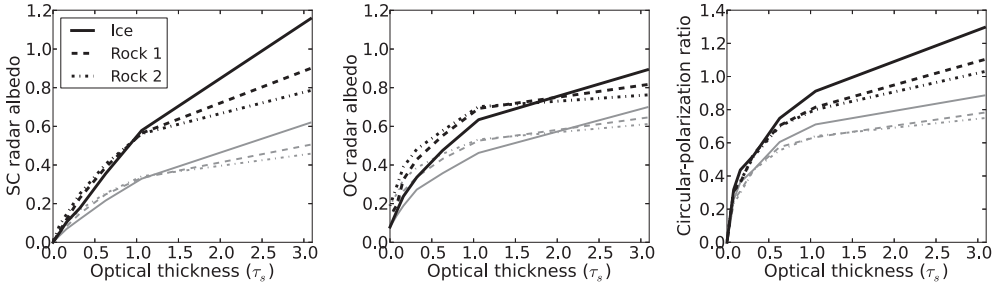

Fig. 10. The SC and OC radar albedo and the circular-polarization ratio as a function of the geometric, optical thickness of a diffuse external medium. The gray lines depict the radiative transfer solution, and the black lines with corresponding line style that including the CBM.

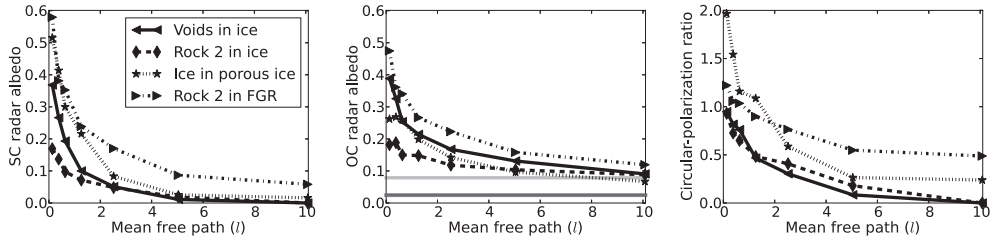

Fig. 11. The SC and OC radar albedo and the circular-polarization ratio as a function of the mean free path in meters when using a diffuse internal medium and including the CBM. The gray horizontal lines at 0.02 (porous/powdered ice or FGR, dark gray) and 0.08 (solid ice, light gray) computed using Eq. (3) depict the OC radar albedo considering only specular scattering, that is, no diffuse medium.

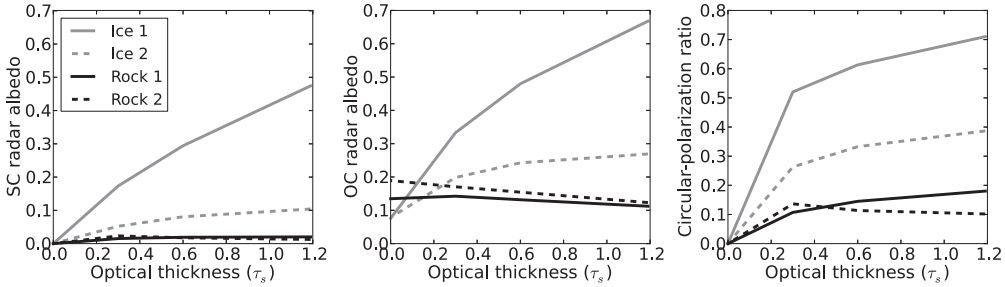

Fig. 12. The SC and OC radar albedo and the circular-polarization ratio as a function of the optical thickness when using large boulders on the surface of the host particle, e.g., an asteroid or an icy satellite.

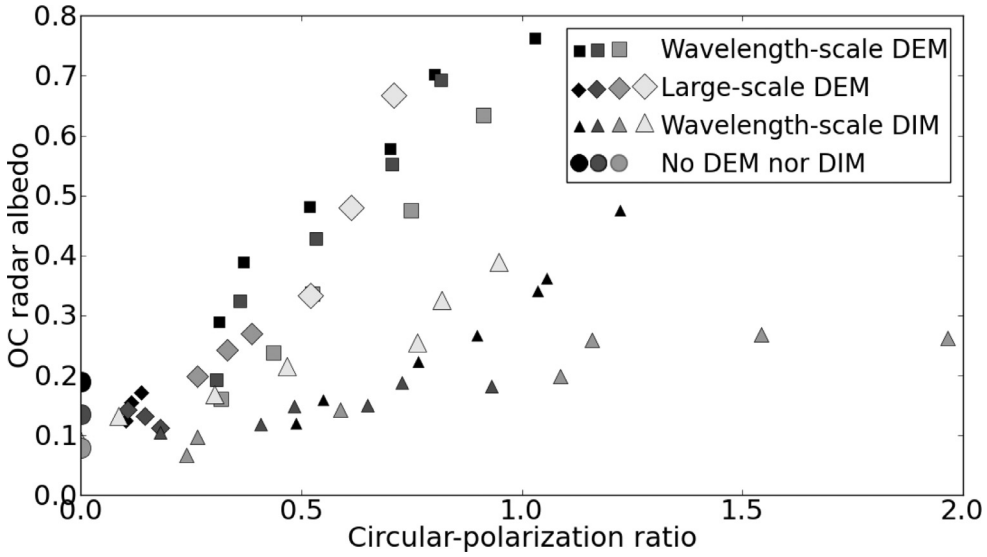

Fig. 13. The OC radar albedos and the circular-polarization ratio modeled using irregular wavelength-scale scatterers as a diffuse external (DEM) or internal medium (DIM) or meter-scale GRS particles as DEM. From left to right, the squares and circles depict rock 2, rock 1, and ice, diamonds depict rock 2, rock 1, absorbing ice, and non-absorbing ice, and triangles depict rock 2 in fine-grained regolith, rock 2 in solid ice, ice grains in porous ice, and voids in solid ice.

approximately 0.04, which corresponds to an effective Re(m) ≈ 1.5. The maximum values of $\hat{\sigma}_{\mathrm{OC}}$, as well as μ_C, are obtained using a large optical thickness, that is, in practice, a large number of surface scatterers.

NEAs have been observed to have higher mean circular-polarization ratios than MBAs (Benner et al., 2008). This fact is not evident in our sample because the number of NEAs with published radar albedos is only 10% of those in the main-belt population; therefore we will not discuss the difference here in further detail. However, the results support that, in average, the surfaces of the NEAs are likely more covered with wavelength-scale rubble than those of the MBAs.

For C-complex asteroids, the mean observed $\hat{\sigma}_{\mathrm{OC}} \approx 0.12 \pm 0.05$ and $\mu_C \approx 0.19 \pm 0.08$ (using error of 1σ). Our model suggests either very low number density of wavelength-scale scatterers on the surface and/or mainly large boulders if any. For the S-complex asteroids, the mean observed $\hat{\sigma}_{\mathrm{OC}} \approx 0.15 \pm 0.04$ and $\mu_C \approx 0.25 \pm 0.09$, which implies slightly more wavelength-scale scatterers than for the C-complex asteroids. For (25143) Itokawa, observed μ_C varies between 0.26 ± 0.04 (Ostro et al., 2004) and 0.48 ± 0.10 (Ostro et al., 2005). As images of Hayabusa show (Saito et al., 2006), the surface of Itokawa has plenty of variation in the size distribution of boulders; therefore the observed values can depend to great extent on the orientation of the asteroid during the observations.

Comets do not differ significantly from the C and S complexes in terms of $\hat{\sigma}_{\mathrm{OC}}$, but the observed values of μ_C vary from 0.105 ± 0.005 (C/IRAS-Araki-Alcock) (Harmon et al., 1989) to 0.59 ± 0.04 (C/2004 Q2 Machholz) (Nolan et al., 2005). The images of Rosetta spacecraft of comet 67P/Churyumov–Gerasimenko present a very irregular surface where the size scales of the geometric structures greatly vary: both very smooth and very rough areas are present, which implies that the wide range of observed values of μ_C could be explained by differences in the surface structure. However, further research concentrating specifically on cometary surfaces is required due to constantly growing knowledge of the mineralogic differences between asteroids and comets.

The X complex includes asteroids with high and low metal content. The M-type asteroids differ in terms of composition greatly from the P- and E-type asteroids. Those with high metal content, we exclude from the model as explained in Section 3.1. The most interesting type of the X complex is the E type, for which only relatively high values of $\hat{\sigma}_{\mathrm{OC}}$ and μ_C have been measured, i.e., mean values of 0.26 ± 0.11 and 0.74 ± 0.27, respectively. The best fit is in the case of internal scatterers rock 2 in FGR using $l \approx 2$ m, i.e., powdered regolith with inclusions of solid wavelength-scale rock scatterers, possibly with moderate metal content but not specifically high. This conclusion is in a good agreement with the hypothesis that the E-type asteroids are associated with the enstatite achondrites (Zellner et al., 1977), which have a brittle tenacity (Sinkankas, 1966), and thus, easily fragment into smaller grains. Furthermore, the conclusion is in agreement with the observed sharp opposition effects and polarization surges in the visible

regime of light, explained also by the CBM mechanism (Muinonen et al., 2002).

The V-type asteroids have the second highest mean circular-polarization ratio of all the asteroid taxonomic classes. The V-type asteroids are also known as vestoids, because they are considered to be fragments of (4) Vesta's crust that were detached as a result of a major impact (Binzel and Xu, 1993; Consolmagno and Drake, 1977). Radar observations would thus imply that as a result of the impact, the vestoids are likely covered with impact ejecta including rubble in centimeter-scale.

For any observed target, for which μ_C is high ($>$0.45), also $\hat{\sigma}_{\mathrm{OC}}$ tends to be greater than the mean value for the S or C types which supports the applicability of the model. We can interpret from the model that the asteroid surfaces are mainly solid, or covered with very fine-grained regolith. Extensive coverage of 10 cm-scale or slightly smaller scatterers is a more local than systematic characteristic of asteroid surfaces, especially for the MBAs.

5. Summary

We study the effect of the physical properties of a planetary surface on radar scattering. We mimic a regolith using laboratory-characterized scatterers, which constitute a diffuse medium on the surface of a large host particle or inside it. This choice of geometry is crucial especially for the diffuse external medium, i.e., the surface roughness. We also investigate the roles of the scatterer size, material, and the number density of the external or internal scatterers on radar scattering.

We find that the surface scatterers that enhance the S-band radar echo most effectively are 5-8 cm in diameter. If the scatterers are internal, particles that have diameter of 12–16 cm are the most effective.

The radar reflectivity increases as a function of the number density of the diffuse surface scatterers, or the surface roughness. This applies to both $\hat{\sigma}_{\mathrm{SC}}$ and $\hat{\sigma}_{\mathrm{OC}}$. The rate of increase depends to some extent on the electric properties of the surface, and can therefore be affected by the metal content as well as the near-surface packing density. Also, the CBM enhances the radar observables. The enhancement depends on the number density of scatterers, and it is more substantial for $\hat{\sigma}_{\mathrm{SC}}$ than for $\hat{\sigma}_{\mathrm{OC}}$, which is why the CBM increases μ_C.

For C-complex asteroids, our model suggests either very low number density of wavelength-scale scatterers on the surface and/or mainly large boulders if any. For S-complex asteroids, the model implies slightly more wavelength-scale scatterers than for the C-complex. For E-type asteroids, the abundance of metal has been debated, but in our model, internal rock scatterers in fine-grained regolith using a mean free path of approximately 2 m are the best fit for the high circular-polarization ratio and OC radar albedo.

The scatterer geometry is crucial especially for icy surface scatterers. This implies that extra caution should be taken when modeling radar scattering using ice particles, as the surface geometry may enhance the radar echo unexpectedly. The results support the use of laboratory-characterized scatterers instead of simplified geometries. The radar scattering by the diffuse internal medium is less dependent of the shape of the diffuse scatterers than radar scattering by the diffuse external medium, because of the absorption of the host particle and the differences in the scattering trajectories.

For the Galilean Moon Europa, the icy surface plays a prominent part in the extraordinarily high radar reflectivity and circular polarization ratio. We find that solid ice inclusions in porous/powdered ice reproduce circular-polarization ratios, which are comparable to the observed values. Rock inclusions inside porous/powdered ice are capable of reproducing higher values of radar observables than for example Black et al. (2001) suggest if the absorption of the scatterers is estimated lower. In addition, any surface scatterers can enhance the radar echo.

To conclude, the results are a demonstration of the effects of various physical parameters on radar scattering, and thus, help to explain the variation of the circular-polarization ratios between the different taxonomic groups of asteroids as well as planetary surfaces in general. The greatest challenges of the model are the free parameters, such as the size distributions and absorption, which have been shown to have major effects on the radar echo but can be very diverse in different planetary surfaces. Albeit our model is quantitatively well-established, the future is still open for improvements and thus increasing our understanding of radar scattering.

Acknowledgments

We wish to thank CSC – IT Center for Science for valuable computer resources and Hannakaisa Lindqvist for providing us with the shape models of the dust particles. The research was partly funded by the Academy of Finland project 1257966 and the ERC Advanced Grant no. 320773 entitled Scattering and Absorption of Electromagnetic Waves in Particulate Media (SAEMPL).

References

Benner, L.A.M., Hudson, R.S., Ostro, S.J., et al., 1999. Radar observations of Asteroid 2063 Bacchus. Icarus 139, 309–327.
Benner, L.A.M., Ostro, S.J., Hudson, R.S., et al., 2002. Radar observations of Asteroid 3908 Nyx. Icarus 158, 379–388.
Benner, L.A.M., Ostro, S.J., Magri, C., et al., 2008. Near-Earth asteroid surface roughness depends on compositional class. Icarus 198, 294–304.
Binzel, R.P., Xu, S., 1993. Chips off of asteroid 4 Vesta - Evidence for the parent body of basaltic achondrite meteorites. Science 260, 186–191.
Black, G.J., Campbell, D.B., Nicholson, P.D., 2001. Icy Galilean satellites: modeling radar reflectivities as a coherent backscatter effect. Icarus 151, 167–180.
Bohren, C.F., Huffman, D.R., 1983. Absorption and Scattering of Light by Small Particles. John Wiley & Sons, Inc., USA.
Brozovic, M., Ostro, S.J., Benner, L.A.M., et al., 2009. Radar observations and a physical model of Asteroid 4660 Nereus, a prime space mission target. Icarus 201, 153–166.
Busch, M.W., Ostro, S.J., Benner, L.A.M., et al., 2006. Radar and optical observations and physical modeling of near-Earth Asteroid 10115 (1992 SK). Icarus 181, 145–155.
Campbell, B.A., Carter, L.M., Campbell, D.B., et al., 2010. Earth-based 12.6-cm wavelength radar mapping of the Moon: new views of impact melt distribution and mare physical properties. Icarus 208, 565–573.
Campbell, B.A., Hawke, B.R., Campbell, D.B., 2009. Surface morphology of domes in the Marius Hills and Mons Rümker regions of the Moon from Earth-based radar data. J. Geophys. Res. (Planets) 114, 1001.
Campbell, D.B., Chandler, J.F., Ostro, S.J., et al., 1978. Galilean satellites – 1976 radar results. Icarus 34, 254–267.
Campbell, M.J., Ulrichs, J., 1969. Electrical properties of rocks and their significance for lunar radar observations. J. Geophys. Res. 74, 5867–5881.
Capaccioni, F., Coradini, A., Filacchione, G., 2015. The organic-rich surface of comet 67P/Churyumov-Gerasimenko as seen by VIRTIS/Rosetta. Science 347 (1), aaa0628.
Consolmagno, G.J., Drake, M.J., 1977. Composition and evolution of the eucrite parent body – evidence from rare earth elements. Geochimica et Cosmochimica Acta 41, 1271–1282.
de Pater, I., Palmer, P., Mitchell, D.L., et al., 1994. Radar aperture synthesis observations of asteroids. Icarus 111, 489–502.
Draine, B.T., Flatau, P.J., 1994. Discrete-dipole approximation for scattering calculations. J. Opt. Soc. Am. A 11, 1491–1499.
Garvin, J.B., Head, J.W., Pettengill, G.H., et al., 1985. Venus global radar reflectivity and correlations with elevation. J. Geophys. Res. 90, 6859–6871.
Hapke, B., 1990. Coherent backscatter and the radar characteristics of outer planet satellites. Icarus 88, 407–417.
Harmon, J.K., Campbell, D.B., Hine, A.A., et al., 1989. Radar observations of Comet IRAS-Araki-Alcock 1983d. Astrophys. J. 338, 1071–1093.
Hastie, T.J., Tibshirani, R.J., 1990. Generalized Additive Models. Chapman & Hall, UK.
Hudson, R.S., Ostro, S.J., Jurgens, R.F., et al., 2000. Radar observations and physical model of Asteroid 6489 Golevka. Icarus 148, 37–51.
Hudson, R.S., Ostro, S.J., Scheeres, D.J., 2003. High-resolution model of Asteroid 4179 Toutatis. Icarus 161, 346–355.
Koyama, Y., Nakajima, J., Sekido, M., et al., 2001. Radar observations of near Earth Asteroids 6489 Golevka and 4197 (1982 TA). Commun. Res. Lab. J. 48, 143.
Lindqvist, H., Jokinen, O., Kandler, K., et al., 2014. Single scattering by realistic, inhomogeneous mineral dust particles with stereogrammetric shapes. Atmos. Chem. Phys. 14, 143–157.

Magri, C., Consolmagno, G.J., Ostro, S.J., et al., 2001. Radar constraints on asteroid regolith compositions using 433 Eros as ground truth. Meteorit. Planet. Sci. 36, 1697–1709.
Magri, C., Nolan, M.C., Ostro, S.J., et al., 2007a. A radar survey of main-belt asteroids: Arecibo observations of 55 objects during 1999–2003. Icarus 186, 126–151.
Magri, C., Ostro, S.J., Rosema, K.D., et al., 1999. Mainbelt asteroids: results of Arecibo and Goldstone Radar observations of 37 objects during 1980–1995. Icarus 140, 379–407.
Magri, C., Ostro, S.J., Scheeres, D.J., et al., 2007b. Radar observations and a physical model of Asteroid 1580 Betulia. Icarus 186, 152–177.
Mishchenko, M.I., 1992. Polarization characteristics of the coherent backscatter opposition effect. Earth Moon Planets 58, 127–144.
Mishchenko, M.I., 1996. Diffuse and coherent backscattering by discrete random media. I. Radar reflectivity, polarization ratios, and enhancement factors for a half-space of polydisperse, nonabsorbing and absorbing spherical particles. J. Quant. Spectrosc. Radiat. Transf. 56, 673–702.
Mishchenko, M.I., Hovenier, J.W., 1995. Depolarization of light backscattered by randomly oriented nonspherical particles. Opt. Lett. 20, 1356–1358.
Mitchell, D.L., Ostro, S.J., Hudson, R.S., et al., 1996. Radar observations of Asteroids 1 Ceres, 2 Pallas, and 4 Vesta. Icarus 124, 113–133.
Mitchell, D.L., Ostro, S.J., Rosema, K.D., et al., 1995. Radar observations of asteroids 7 Iris, 9 Metis, 12 Victoria, 216 Kleopatra, and 654 Zelinda.. Icarus 118, 105–131.
Muinonen, K., Mishchenko, M.I., Dlugach, J.M., et al., 2012. Coherent backscattering verified numerically for a finite volume of spherical particles. Astrophys. J. 760, 118.
Muinonen, K., Nousiainen, T., Fast, P., et al., 1996. Light scattering by Gaussian random particles: Ray optics approximation. J. Quant. Spectrosc. Radiat. Transf. 55, 577–601.
Muinonen, K., Nousiainen, T., Lindqvist, H., 2009. Light scattering by Gaussian particles with internal inclusions and roughened surfaces using ray optics. J. Quant. Spectrosc. Radiat. Transf. 110, 1628–1639.
Muinonen, K., Piironen, J., Shkuratov, Y.G., 2002. Asteroid photometric and polarimetric phase effects. In: Asteroids III. Academic Press, Tucson, USA, pp. 123–138.
Nolan, M.C., Campbell, D.B., Harmon, J.K., 2005. Arecibo radar detection of the nucleus and coma of C/2004 Q2 (Machholz). I. A. U. Symp. 229, 120.
Ostro, S.J., Benner, L.A.M., Magri, C., 2005. Radar observations of Itokawa in 2004 and improved shape estimation. Meteorit. Planet. Sci. 40, 1563–1574.
Ostro, S.J., Benner, L.A.M., Nolan, M.C., 2004. Radar observations of asteroid 25143 Itokawa (1998 SF36). Meteorit. Planet. Sci. 39, 407–424.
Ostro, S.J., Campbell, D.B., Shapiro, I.I., 1983. Radar observations of asteroid 1685 Toro. Astron. J. 88, 565–576.
Ostro, S.J., Campbell, D.B., Shapiro, I.I., 1985. Mainbelt asteroids – dual-polarization radar observations. Science 229, 442–446.
Ostro, S.J., Campbell, D.B., Simpson, R.A., 1992. Europa, Ganymede, and Callisto – new radar results from Arecibo and Goldstone. J. Geophys. Res. 97, 18227.
Ostro, S.J., Hudson, R.S., Benner, L.A.M., 2002. Asteroid radar astronomy. In: Bottke Jr, W.F., Cellino, A., Paolicchi, P., Binzel, R.P. (Eds.), Asteroids III. Academic Press, Tucson, USA, pp. 151–180.
Ostro, S.J., Hudson, R.S., Rosema, K.D., et al., 1999. Asteroid 4179 Toutatis: 1996 radar observations. Icarus 137, 122–139.
Ostro, S.J., Nolan, M.C., Margot, J.-L., et al., 2001. Radar observations of Asteroid 288 Glauke. Icarus 152, 201–204.
Ostro, S.J., Rosema, K.D., Campbell, D.B., et al., 1991. Asteroid 1986 DA – radar evidence for a metallic composition. Science 252, 1399–1404.
Ostro, S.J., Yeomans, D.K., Chodas, P.W., et al., 1989. Radar observations of asteroid 1986 JK. Icarus 78, 382–394.
Peltoniemi, J.I., Lumme, K., Muinonen, K., et al., 1989. Scattering of light by stochastically rough particles. Appl. Opt. 28, 4088–4095.
Penttilä, A., Lumme, K., 2011. Optimal cubature on the sphere and other orientation averaging schemes. J. Quant. Spectrosc. Radiat. Transf. 112, 1741–1746.
Peters, K.J., 1992. Coherent-backscatter effect – a vector formulation accounting for polarization and absorption effects and small or large scatterers. Phys. Rev. B – Condens. Matter, 3rd Ser. 46, 801–812.
Rayleigh, L., 1892. On the influence of obstacles arranged in rectangular order on the properties of a medium. Philos. Mag. 34, 481–502.
Saito, J., Miyamoto, H., Nakamura, R., et al., 2006. Detailed images of Asteroid 25143 Itokawa from Hayabusa. Science 312, 1341–1344. doi:10.1126/science.1125722.
Shepard, M.K., Clark, B.E., Nolan, M.C., et al., 2008a. Multi-wavelength observations of Asteroid 2100 Ra-Shalom. Icarus 193, 20–38.
Shepard, M.K., Clark, B.E., Nolan, M.C., et al., 2008b. A radar survey of M- and X-class asteroids. Icarus 195, 184–205.
Shepard, M.K., Clark, B.E., Ockert-Bell, M., et al., 2010. A radar survey of M- and X-class asteroids II. Summary and synthesis. Icarus 208, 221–237.
Shepard, M.K., Taylor, P.A., Nolan, M.C., et al., 2015. A radar survey of M- and X-class asteroids. III. Insights into their composition, hydration state, and structure. Icarus 245, 38–55.
Shoemaker, E.M., Morris, E.C., 1968. Size-Frequency Distribution of Fragmental Debris, Surveyor Project Final Report. Technical Report 32-1265. NASA.
Sinkankas, J., 1966. Mineralogy: A first Course. D.van Nostrand, Toronto, New york.
Spence, L.B., Morgan, T.J., Sharma, J., 1997. Haystack Radar Observation of the Asteroid Toutatis. Lincoln Laboratory Project Report PSI-188. M.I.T.
Tatsuhiro Michikami, T., Nakamura, A.M., Hirata, N., et al., 2008. Size-frequency statistics of boulders on global surface of asteroid 25143 Itokawa. Earth Planets Space 60, 13–20.
Tsang, L., Kong, J.A., Shin, R.T., 1985. Theory of Microwave Remote Sensing. Wiley, New York, USA.
van de Hulst, H.C., 1981. Light Scattering by Small Particles. Dover Publications, New York, USA.
Virkki, A., Muinonen, 2015a. Polarized backscattering by clusters of spherical particles. Opt. Lett. 40 (16), 3663–3666.
Virkki, A., Muinonen, 2015b. Radar scattering by boulders studied using geometric optics. Planet. Space Sci. 118, 277–284.
Virkki, A., Muinonen, K., Penttilä, A., 2013. Circular polarization of spherical-particle aggregates at backscattering. J. Quant. Spectrosc. Radiat. Transf. 126, 150–159.
Virkki, A., Nolan, M., Taylor, P., et al., 2014. Circular-polarization ratio variation with rotation for 2006 AM_4. In: Muinonen, K., Penttilä, A., Granvik, M., Virkki, A., Fedorets, G., Wilkman, O., Kohout, T. (Eds.), Asteroids, Comets, Meteors 2014. University of Helsinki, Helsinki, p. 568.
Warren, S.G., 2008. Optical constants of ice from the ultraviolet to the microwave: A revised compilation. J. Geophys. Res. 113, D14220.
Yurkin, M.A., Hoekstra, A.G., 2011. The discrete-dipole-approximation code ADDA: capabilities and known limitations. J. Quant. Spectrosc. Radiat. Transf. 112, 2234–2247.
Zaitsev, A.L., Ostro, S.J., Ignatov, S.P., et al., 1997. Intercontinental bistatic radar observations of 6489 Golevka (1991 JX). Planet. Space Sci. 45, 771–778.
Zellner, B., Leake, M., Williams, J.G., et al., 1977. The E asteroids and the origin of the enstatite achondrites. Geochim. Cosmochim. Acta 41, 1759–1767.